CONVECTION DRIVEN FLOW BETWEEN MOVING DISKS- A NON-LINEAR APPROACH FOR MODELLING THERMAL RADIATION

Kashif ALI
Department of Basic Science and Humanities, Muhammad Nawaz Sharif University of Engineering & Technology, Multan 60000, Pakistan.

kashifali_381@yahoo.com

Anique AHMAD
Centre for Advanced Studies in Pure & Applied Mathematics, Bahauddin Zakariya University, Multan 60800, Pakistan.

aniqueahmad19@gmail.com

Shahzad AHMAD*
Centre for Advanced Studies in Pure & Applied Mathematics, Bahauddin Zakariya University, Multan 60800, Pakistan.

Corresponding author; shahzadahmad@bzu.edu.pk

Abstract

Flows involving two disks have significant applications in heat exchangers, rotating machinery parts, data storage devices, oceanography and viscometers. In this investigation, heat and mass transfer characteristics are examined in Casson flow between two orthogonally moving disks, with nonlinear thermal radiation under the slip and convective conditions, using the powerful tool of similarity transformation. A MATLAB code, based on quasi-linearization, has been developed for the numerical study. It is observed that, when the disks are receding, the disk expansion ratio raises the velocity profile near the center of the region between the two disks. The trend is, however, reversed when the disks are approaching each other. Moreover, all the governing parameters remarkably elevate the fluid temperature at a central region between the disks, for both cases. A remarkable lowering in concentration distribution is also noted with the Schmidt number and the chemical reaction parameter. Finally, compared to thermal and concentration profiles, it is the velocity distribution which is least affected.

Keywords: Non-linear thermal radiation, Casson fluid, Chemical reaction, Slip and convective boundary conditions, Expanding or Contracting disk, Numerical solution.

1. Introduction

Heat and mass transfer aspects in the existence of chemical reaction through various geometries have fascinated the interest of the researcher community due to its substantial and tremendous applications in numerous fields that contain the damage of crop due to freezing, transfer of energy distribution in a wet cooling tower, grooves of fruit trees, spreading of moisture in agricultural fields, and flow in a desert cooler [1]. Rotor-stator system has achieved great awareness for convection of heat transfer in power engineering, air cleaning machine, and several turbomachinery applications. Numerous researchers have put their best effort into disk-related problems with various wall conditions. Von Karman [2] was the first who initiate the study of flow by a rotating disk. He converted the Navier–Stokes governing equations into ordinary differential equations (ODEs). Afterward, numerous researchers adopted the Karman transformations to investigate various problems. By employing the Successive over Relaxation (SOR) technique, Abbas et al. [3] studied an incompressible, viscous, and non-Newtonian flow over the oscillatory/rotating disk with porous media. They perceived that an increment in porosity parameters results in decelerating the oscillatory velocity.

The viscoelastic nanofluid flow consists of gyrotactic microorganisms (GM) over a rotating stretching disk taking into account the zero mass flux and convective boundary conditions were studied by Abbasi et al. [4]. The influence of prominent parameters on both azimuthal and radial velocities, concentration, temperature, and density of motile-microorganisms for convective and non-convective surfaces was discussed thoroughly. Thermo-physical properties of Newtonian fluid over a rotating disk were investigated by Mair et al. [5]. The fifth-order Rung-Kutta-Fehlberg (RKF) integration technique was implemented to discuss the new findings. They noticed that the concentration and temperature distribution enhanced with thermal diffusivity and conductivity. Magnetohydrodynamics (MHD) Carreau fluid containing nanoparticles with GM over a heated disk with the existence of Brownian motion and thermophoresis were examined by Muhammad et al. [6].

By incorporating the optimal homotopic analysis method (HAM), Adil et al. [7] discussed the impact of thermal and velocity slip in Darcy-Forchheimer flow in a rotating disk taking into account the viscous dissipation. They found that the skin friction is accelerated by the velocity slip parameters and the heat transfer rate is augmented with the thermal slip and Eckert number. Mamatha et al. [8] studied the characteristics of heat transfer between porous and nonporous rotating disks with graphene as nanoparticle in water and ethylene glycol-based fluid. The RK method based on shooting technique was implemented to find the characteristics of sundry variables. They found that augmentation in Hartman number decelerates the wall friction in tangential and radial directions.

Jawad et al. [9] studied the unsteady Maxwell fluid due to horizontal rotating disks in the existence of nanoparticles. A finite-difference-based computational scheme was incorporated for the solution procedure. They concluded that nanofluid film thickness decelerated with the magnetic parameter, unsteadiness parameter, and Deborah number. Moreover, the rate of mass transfer was augmented with the thermophoresis. Babu et al. [10] investigated the numerical modelling of activation energy in MHD Casson fluid flow via stretchable rotating disk. For the understanding of complex interaction of Lorentz and Coriolis forces in EMHD power law fluid inside a micro-channel was investigated by Ali et al. [11].

A new kind of non-Newtonian fluid (Reiner-Rivlin) over a rough rotating disk under different slip conditions was studied by Syed et al. [12]. They observed that for a large wall slip, a higher value of torque was required under continuous rotating disk. Iqbal et al. [13-14] studied the mass and heat transport aspects in unsteady electrically conducting MHD nanofluid between two porous moving disks.

Buongiorno's model for the assessment of transient flow in Maxwell nanofluid through a vertically moving disk were presented by Masood et al. [15]. Additionally, the influence of Lorentz force produced by magnetic field acted normally to the direction of flow was also investigated. They found that the disk motion (upward or downward) exerts a similar effect to that of the injection/suction through the wall and the heat transfer rate raises remarkably with the spin. Muhammad et al. [16] studied the heat transport phenomenon in viscous fluid flow due to flexible rotating disks with the Dufour and Soret effect.

Thermal radiation assumes a major contribution in manufacturing industries for atomic power plant designing and modeling applications. Due to its important applications, numerous scientists and engineers have given their deliberation to thermal radiation impact. Moreover, heat convection plays a dynamic role in industrial applications such as solar ponds, and metal solidification processes. Heat convection is also used in several biomedical fields such as the destruction of tumors and laser treatment of the cornea. Taza et al. [17] discussed the thermal analysis of a hybrid nanofluid between a cone and a disk under the effect of the imposed magnetic field. Two distinct types of hybrid nanoparticles such as copper and magnetic ferrite were considered in this novel study. They found that an increment in volume fraction increases the rate of thermal diffusion. Talat et al. [18] considered the unsteady revolving fluid flow generated by a rotating porous disk with temperature-dependent viscosity. Two different numerical schemes such as modified finite difference and the collocation method were employed to find the solutions of the problem. They found that variable thermal conductivity considerably alters the heat transfer rate and drag coefficient.

Khan et al. [19] examined the hybrid nanofluid flow near the stagnation point with the arched surface. Hussain et al [20] studied the hybrid base nano watery flow over an exponentially rotating stretching sheet with the convective boundary conditions. Li et al. [21] investigated the transport of heat and mass in MHD Williamson nanofluid over an exponentially permeable elongating sheet. The heat transfer characteristics and skin friction for stagnation point flow with two types of carbon nanotubes (single- walled and multi- walled carbon nanotubes) based nanofluid flowing over a curved surface was deliberated by Khan et al. [22].

Casson fluid model has been broadly used for studying diverse applications concerning the flow of yield stress fluids. Casson fluid belongs to a non-Newtonian fluid because of its rheological nature relating to the shear stress and strain relationship. The general model of liquids that shows the characteristics of Casson fluid are human blood, soup, orange juice, and tomato sauce. Activation energy in Darcy–Forchheimer flow of non-Newtonian fluid with nanoparticles (Titanium dioxide and Graphene oxide) in a permeable medium was studied by Naveen et al. [23]. Mathematical problem was solved by implementing the RKF-45 method along with the shooting technique. They found that an increment in the Casson parameter remarkably decelerates the fluid velocity.

Zhao et al. [24] examined the entropy generation analysis in MHD flow of Ree-Eyring fluid between two rotating disks. From this study, it is observed that the Bejan number and entropy generation have totally contradictory trends against higher values of Weissenberg number. Ghaffar et al. [25] studied an unsteady laminar incompressible flow between two disks and different physical quantities of interest were discussed in detail. Rheological features of Casson-Maxwell nanofluids over stretchable rotating disk was studied by Shehzad et al. [26]. Moreover, a well-known Buongiorno theory of nanomaterials was employed to illustrate the thermophoresis and Brownian motion effect. To explore the features of peristaltic pumping of MHD Casson fluid in a channel geometry with slip conditions was presented by Ali et al. [27].

Energy conversion to improve the heat production during the flow of ternary hybrid nanofluid contained nanoparticles over a spinning disk by considering the radiation and Hall current impacts was reported by Shamshuddin et al. [28]. Ahmad et al. [29] demonstrated the steady MHD boundary layer flow of an electrically conducting micropolar fluid over an inclined surface. Jawad et al. [30] studied the unsteady non Newtonian fluid between two orthogonally moving porous disks. To solve the coupled nonlinear equations, the RK method is utilized. Various parameters effects are discussed in detail.

Further relevant research regarding the flows driven by the moving disks can be seen through the investigations [13-14] and the references therein. To the authors' best knowledge, no mathematical modeling and the consequent numerical solution has been obtained for understanding the cumulative impact of nonlinear thermal radiation, viscous dissipation, and chemical reaction on unsteady MHD Casson fluid between two orthogonally moving porous disks. Furthermore, velocity slip and thermal convective conditions at the boundary are imposed in this model. The highly nonlinear PDEs are transmuted into ODEs via similarity transformation and then numerically solved by incorporating the quasi-linearization technique in the MATLAB environment. Our numerical technique is also different from the usual shooting methodology being employed by many researchers. Results reveal that the fluid flow is affected by preeminent parameters. Outcome of the present investigation not only provides essential information to mechanical applications, but also discusses the suitability of our computational approach for the self-similar flow problems.

2. Problem formulation

Take a two-dimensional unsteady electrical conducting hydromagnetic viscous and incompressible Casson fluid flow between two orthogonally moving porous disks, in the existence of an applied magnetic field. Here, we considered that the induced magnetic field is small related to the imposed one. We also supposed that the magnetic Reynolds number is very small. It is also considered that there is no polarization and thus no electric field. Since both disks have similar permeability, to uniformly move up or down at a time-dependent rate $L'(t)$.

The upper and lower disks are at the specific distance of $L(t)$ and $-L(t)$ from the horizontal axis respectively as shown in Figure 1. A suitable cylindrical polar coordinates system is established at the center of the two disks. The velocity components are u_1 and u_3 in the r and z directions, respectively.

For an isotropic flow, the equation of the rheological state of a Casson fluid can be demonstrated as:

$$\tilde{\tau}_{ij} = \begin{cases} 2\left(\dfrac{\tilde{\mu}_B + P_y}{\sqrt{2\tilde{\pi}}}\right)\tilde{e}_{ij}, & \tilde{\pi} > \tilde{\pi}_C, \\ 2\left(\dfrac{\tilde{\mu}_B + P_y}{\sqrt{2\tilde{\pi}_c}}\right)\tilde{e}_{ij}, & \tilde{\pi} > \tilde{\pi}_C, \end{cases} \tag{1}$$

In Equation (1), $\tilde{\pi} = \tilde{e}_{ij}\tilde{e}_{ij}$, here $\tilde{e}_{ij}$ is the $(i,j)^{th}$ deformation rate component. This implies the definition of $\tilde{\pi}$ which is the product of the deformation rate with itself and the critical value for this product based is $\tilde{\pi}_c$. Also, P_y and $\tilde{\mu}_B$ are the yield stress and the fluid dynamic viscosity.

Momentum, heat and mass transfer equations in cylindrical polar coordinates system (r, θ, z) under slip and convective conditions taking chemical reaction, viscous dissipation, and nonlinear thermal radiation into accounts are

$$\frac{\partial u_1}{\partial r} + \frac{u_1}{r} + \frac{\partial u_3}{\partial z} = 0, \tag{2}$$

$$\frac{\partial u_1}{\partial t} + u_1\frac{\partial u_1}{\partial r} + u_3\frac{\partial u_1}{\partial z} = -\frac{1}{\rho}\frac{\partial p}{\partial r} + \upsilon\left(1+\frac{1}{\beta}\right)\left(\frac{\partial^2 u_1}{\partial r^2} + \frac{1}{r}\frac{\partial u_1}{\partial r} - \frac{u_1}{r^2} + \frac{\partial^2 u_1}{\partial z^2}\right) - \frac{\sigma_e \mathrm{B}_0^2 u_1}{\rho}, \tag{3}$$

$$\frac{\partial u_3}{\partial t} + u_1\frac{\partial u_3}{\partial r} + u_3\frac{\partial u_3}{\partial z} = -\frac{1}{\rho}\frac{\partial p}{\partial z} + \upsilon\left(1+\frac{1}{\beta}\right)\left(\frac{\partial^2 u_3}{\partial r^2} + \frac{1}{r}\frac{\partial u_3}{\partial r} + \frac{\partial^2 u_3}{\partial z^2}\right), \tag{4}$$

$$\frac{\partial T}{\partial t}+u_1\frac{\partial T}{\partial r}+u_3\frac{\partial T}{\partial z}=\tilde{\alpha}\frac{\partial^2 T}{\partial z^2}+\frac{\mu}{(\rho c_p)}\left(1+\frac{1}{\beta}\right)\left(\frac{\partial u_1}{\partial z}\right)^2-\frac{1}{\rho c_p}\frac{4\sigma^*}{3k^*}\frac{\partial^2 T^4}{\partial z^2}+\frac{\sigma_e B_0^2 u_1^2}{\rho}, \tag{5}$$

$$\frac{\partial C}{\partial t}+u_1\frac{\partial C}{\partial r}+u_3\frac{\partial C}{\partial z}=-K_1(C-C_2)+D\,\nabla^2 C. \tag{6}$$

here σ_e is the electrical conductivity, ρ is the density, B_0 represented as the applied magnetic field, the thermal conductivity is denoted by $\tilde{\alpha}$, υ is the kinematics viscosity, T and C are illustrated as fluid temperature and concentration, respectively.
Boundary conditions are:

$$\left.\begin{aligned} z=-L(t);\ u_1=u_{slip},\ u_3=-HL'(t),\ -k\left(\frac{\partial T}{\partial z}\right)=h_1(T_1-T),\ C=C_1,\\ z=L(t);\ u_1=0,\ u_3=HL'(t),\ -k\left(\frac{\partial T}{\partial z}\right)=h_2(T-T_2),\ C=C_2.\end{aligned}\right\} \tag{7}$$

here, $u_{slip}=-\frac{\sqrt{k}}{\alpha_0}\left(\frac{\partial u}{\partial r}\right)$ is a slip velocity, the wall permeability is H, and the prime represents the derivative w.r.t time t, $T_1,\ T_2$ demonstrate the fixed temperatures (with $T_1>T_2$), h_1, h_2 represents the coefficient of convective heat transfer and C_1, C_2 represents a fixed concentration, respectively. We consider the temperature difference along the flow such that T^4 can be written as a linear function of the temperature. By expanding T^4 through Taylors series expansion around T_∞ and truncating higher-order expressions as,

$$T^4\cong 4T_\infty^3 T-3T_\infty^4. \tag{8}$$

With the implication of the nonlinear Rosseland diffusion approximation,

$$\frac{\partial^2 T^4}{\partial z^2}=4T^3\frac{\partial^2 T}{\partial z^2}+12T^2\left(\frac{\partial T}{\partial z}\right)^2, \tag{9}$$

yields

$$\frac{\partial T}{\partial t}+u_1\frac{\partial T}{\partial r}+u_3\frac{\partial T}{\partial z}=\left(\alpha+\frac{1}{\rho c_p}\frac{16\sigma^* T_\infty^3}{3k^*}\right)\frac{\partial^2 T}{\partial z^2}+\frac{\mu}{(\rho c_p)}\left(1+\frac{1}{\beta}\right)\left(\frac{\partial u_1}{\partial z}\right)^2+\frac{1}{\rho c_p}\frac{48\sigma^* T_\infty^2}{3k^*}\left(\frac{\partial T}{\partial z}\right)^2+\frac{\sigma_e B_0^2 u_1^2}{\rho}, \tag{10}$$

here σ^* and k^* are the Stefan-Boltzmann constant and absorption coefficient.
Following similarity transformations are proposed for the conversion of PDEs into the corresponding non-linear ODEs.

$$\xi=\frac{z}{L},\ \ u_1=-\frac{r\upsilon}{L^2}F_\xi(\xi,t),\ u_3=\frac{2\upsilon}{L}F_\xi(\xi,t),\ \theta(\xi,t)=\frac{T-T_2}{T_1-T_2},\ \ \phi(\xi,t)=\frac{C-C_2}{C_1-C_2}, \tag{11}$$

after omitting the pressure term, we get

$$\left(1+\frac{1}{\beta}\right)F_{\xi\xi\xi\xi}+\left(3F_{\xi\xi}+\xi F_{\xi\xi\xi}\right)\alpha-\frac{L^2}{\upsilon_f}F_{\xi\xi t}-2FF_{\xi\xi\xi}-MF_{\xi\xi}=0\cdot \tag{12}$$

$$\left(1+\frac{4}{3}N_r(1+\varepsilon\theta)^3\right)\theta_{\xi\xi}+4Nr(1+\varepsilon\theta)^2\theta_\xi^2+\Pr(\xi\alpha-2F)\theta_\xi+\left(1+\frac{1}{\beta}\right)\Pr Ec\left(F_{\xi\xi}^2+MF_\xi{}^2\right)-\frac{L^2}{\alpha}\theta_t=0\cdot$$

(13)

$$\phi_{\xi\xi}+Sc(\xi\alpha+2F)\phi_\xi+\frac{a^2}{D}\phi_\xi+\gamma Sc\phi=0, \tag{14}$$

with transformed BCs:

$$\left.\begin{array}{l}\xi=-1;\quad F=-\mathrm{Re},\ \ F_{\xi}=-\lambda F_{\xi\xi},\quad \theta'(-1,\xi)=-\delta\left(1-\theta(-1,\xi)\right),\ \phi=1,\\ \xi=1;\quad F=\mathrm{Re},\quad F_{\xi}=0,\quad \theta'(1,\xi)=-\delta\theta(1,\xi),\ \ \phi=0.\end{array}\right\},\tag{15}$$

here $\alpha, M, \mathrm{Re}, \mathrm{Pr}, Sc, Ec, Nr$ and γ are non-dimensional parameters called, respectively, the wall expansion ratio, magnetic field parameter, Reynolds number, Prandtl number, Schmidt number, Eckert number, thermal radiation, and chemical reaction.

$$\left.\begin{array}{llll}\alpha=\dfrac{LL'(t)}{\upsilon}, & M=\dfrac{\sigma_e B_0^2 L^2}{\mu}, & \mathrm{Re}=\dfrac{HLL'}{2\upsilon}, & \mathrm{Pr}=\dfrac{\mu c_p}{k},\\ Sc=\dfrac{\upsilon}{D}, & Ec=\dfrac{(r\upsilon)^2}{L^4(T_1-T_2)c_p}, & \gamma=\dfrac{L^2K_1}{\upsilon}, & Nr=\dfrac{4\sigma^*}{kk^*}T_1^3.\end{array}\right\}\tag{16}$$

By putting Equation (15) into Equation (2), the continuity equation is satisfied and consequently velocity field signifies the fluid motion. Now by setting, $\underset{\sim}{f}=F/\mathrm{Re}$ and assuming the case for which wall expansion ratio α is constant (please see reference [1]), $\underset{\sim}{f}=\underset{\sim}{f}(\xi)$, $\underset{\sim}{\theta}=\underset{\sim}{\theta}(\xi)$ and $\underset{\sim}{\phi}=\underset{\sim}{\phi}(\xi)$, that guides to $\underset{\sim}{f}_{\xi\xi t}=0,$ $\underset{\sim}{\theta}_t=0$ and $\underset{\sim}{\phi}_t=0$.

$$\left(1+\frac{1}{\beta}\right)\underset{\sim}{f}_{\xi\xi\xi\xi}+\left(3\underset{\sim}{f}_{\xi\xi}+\xi\underset{\sim}{f}_{\xi\xi\xi}\right)\alpha-2\,\mathrm{Re}\,\underset{\sim}{f}\ \underset{\sim}{f}_{\xi\xi\xi}-M\underset{\sim}{f}_{\xi\xi}=0\tag{17}$$

$$\left(1+\frac{4}{3}N_r\left(1+\varepsilon\underset{\sim}{\theta}\right)^3\right)\underset{\sim}{\theta}_{\xi\xi}+4Nr\left(1+\varepsilon\underset{\sim}{\theta}\right)^2\underset{\sim}{\theta}_{\xi}^2+\mathrm{Pr}\left(\xi\alpha-2\,\mathrm{Re}\,\underset{\sim}{f}\right)\underset{\sim}{\theta}_{\xi}+\mathrm{Re}^2\left(1+\frac{1}{\beta}\right)\mathrm{Pr}\,Ec\left(\underset{\sim}{f}_{\xi\xi}^2+M\underset{\sim}{f}_{\xi}^2\right)=0,$$

(18)

$$\underset{\sim}{\phi}_{\xi\xi}+Sc\left(\xi\alpha-2\,\mathrm{Re}\,\underset{\sim}{f}\right)\underset{\sim}{\phi}_{\xi}-\gamma Sc\underset{\sim}{\phi}=0.\tag{19}$$

With associated BCs:

$$\left.\begin{array}{l}\xi=-1;\quad \underset{\sim}{f}=-1,\quad \underset{\sim}{f}_{\xi}=-\lambda\underset{\sim}{f}_{\xi\xi},\quad \underset{\sim}{\theta}'(-1,\xi)=-\delta\left(1-\underset{\sim}{\theta}(-1,\xi)\right),\ \underset{\sim}{\phi}=1,\\ \xi=1;\quad \underset{\sim}{f}=1,\quad \underset{\sim}{f}_{\xi}=0,\quad \underset{\sim}{\theta}'(1,\xi)=-\delta\,\underset{\sim}{\theta}(1,\xi),\ \ \underset{\sim}{\phi}=0.\end{array}\right\}\tag{20}$$

3. Methodology

We apply the quasi-linearization method to solve the converted Equations (17) – (19). For this intention, we make vector sequences of the transformed functions $\left\{\underset{\sim}{f}^{(p)}\right\},\left\{\underset{\sim}{\theta}^{(p)}\right\}$ and $\left\{\underset{\sim}{\phi}^{(p)}\right\}$, which converge to the approximate solution of a dimensionless system.

As per our previous researches related to the solution of nonlinear equations, Quasi-linearization approach has been found to be very efficient to solve the governing converted Equations (17) – (19). The technique is based on the construction of the vector sequences $\left\{\underset{\sim}{f}^{(p)}\right\},\left\{\underset{\sim}{\theta}^{(p)}\right\}$ and $\left\{\underset{\sim}{\phi}^{(p)}\right\}$, converging to the required numerical solution. The construction is detailed as under:

$$Q(\underset{\sim}{f},\underset{\sim}{f}_{\xi},\underset{\sim}{f}_{\xi\xi},\underset{\sim}{f}_{\xi\xi\xi},\underset{\sim}{f}_{\xi\xi\xi\xi})=\left(1+\frac{1}{\beta}\right)\underset{\sim}{f}_{\xi\xi\xi\xi}+\left(3\underset{\sim}{f}_{\xi\xi}+\xi\underset{\sim}{f}_{\xi\xi\xi}\right)\alpha-2\,\mathrm{Re}\,\underset{\sim}{f}\underset{\sim}{f}_{\xi\xi\xi}-M\underset{\sim}{f}_{\xi\xi}$$

$$\left.\begin{array}{l}Q(\underset{\sim}{f}^{(p)},\underset{\sim}{f}_{\xi}^{(p)},\underset{\sim}{f}_{\xi\xi}^{(p)},\underset{\sim}{f}_{\xi\xi\xi}^{(p)},\underset{\sim}{f}_{\xi\xi\xi\xi}^{(p)})+\left(\underset{\sim}{f}^{(p+1)}-\underset{\sim}{f}^{(p)}\right)\dfrac{\partial Q}{\partial\underset{\sim}{f}^{(p)}}+\left(\underset{\sim}{f}_{\xi}^{(p+1)}-\underset{\sim}{f}_{\xi}^{(p)}\right)\dfrac{\partial Q}{\partial\underset{\sim}{f}_{\xi}^{(p)}}\\ +\left(\underset{\sim}{f}_{\xi\xi}^{(p+1)}-\underset{\sim}{f}_{\xi\xi}^{(p)}\right)\dfrac{\partial Q}{\partial\underset{\sim}{f}_{\xi\xi}^{(p)}}+\left(\underset{\sim}{f}_{\xi\xi\xi}^{(p+1)}-\underset{\sim}{f}_{\xi\xi\xi}^{(p)}\right)\dfrac{\partial Q}{\partial\underset{\sim}{f}_{\xi\xi\xi}^{(p)}}+\left(\underset{\sim}{f}_{\xi\xi\xi\xi}^{(p+1)}-\underset{\sim}{f}_{\xi\xi\xi\xi}^{(p)}\right)\dfrac{\partial Q}{\partial\underset{\sim}{f}_{\xi\xi\xi\xi}^{(p)}}\\ \left(1+\dfrac{1}{\beta}\right)\underset{\sim}{f}_{\xi\xi\xi\xi}^{(p+1)}+\left(\xi\alpha-2\,\mathrm{Re}\,\underset{\sim}{f}^{(p)}\right)\underset{\sim}{f}_{\xi\xi\xi}^{(p+1)}+(3\alpha-M)\,\underset{\sim}{f}_{\xi\xi}^{(p+1)}-2\,\mathrm{Re}\,\underset{\sim}{f}_{\xi\xi\xi}^{(p)}\underset{\sim}{f}^{(p+1)}=-2\,\mathrm{Re}\,\underset{\sim}{f}_{\xi\xi\xi}^{(p)}\underset{\sim}{f}^{(p)},\end{array}\right\},\tag{21}$$

We thus obtain the system of differential equations which, on the introduction of central differences for the derivatives, yield the following linear algebraic system:

$$G_{n\times n}\left(\underset{\sim}{f}^{(p)}\right).\underset{\sim}{f}^{(p+1)}=H_{n\times 1}\left(\underset{\sim}{f}^{(p)}\right), \tag{22}$$

with n being the number of grid points (resulting into giving rise to the $n\times n$ algebraic system. It is to point out that no linearization effort is required for the heat and mass treansfer equations, as the two equations are already linear for their corresponding unknowns. Therefore,
the sequences $\left\{\underset{\sim}{\theta}^{(p)}\right\}$ and $\left\{\underset{\sim}{\phi}^{(p)}\right\}$ are given by:

$$\left(1+\frac{4}{3}N_r\right)\underset{\sim}{\theta}_{\xi\xi}^{(p+1)}+\Pr\left(\xi\alpha-2\operatorname{Re}\underset{\sim}{f}^{(p+1)}\right)\underset{\sim}{\theta}_{\xi}^{(p+1)}+\operatorname{Re}^2\left(1+\frac{1}{\beta}\right)\Pr Ec\left(\underset{\sim}{f}_{\xi\xi}^{(p+1)^2}+M\underset{\sim}{f}_{\xi}^{(p+1)^2}\right)=0, \tag{23}$$

$$\underset{\sim}{\phi}_{\xi\xi}^{(p+1)}+Sc\left(\xi\alpha+2\operatorname{Re}\underset{\sim}{f}^{(p+1)}\right)\underset{\sim}{\phi}_{\xi}^{(p+1)}-\gamma Sc\underset{\sim}{\phi}^{(p+1)}=0, \tag{24}$$

with $\underset{\sim}{f}^{(p+1)}$ being considerd as the known solution of Equation (21). The overall algorithm may be outlined as below:

a) A starting guess for $\underset{\sim}{f}^{(0)},\underset{\sim}{\theta}^{(0)}$ and $\underset{\sim}{\phi}^{(0)}$ is supplied;

b) $\underset{\sim}{f}^{(1)}$ is obtained as a solution of Equation (22);

c) $\underset{\sim}{\theta}^{(1)}$ and $\underset{\sim}{\phi}^{(1)}$ are found from Equations (23) and (24) while assuming $\underset{\sim}{f}^{(1)}$, being the solution of Equation (22), as a known vector;

d) Assuming $\underset{\sim}{f}^{(1)}$, $\underset{\sim}{\theta}^{(1)}$ and $\underset{\sim}{\phi}^{(1)}$ as knowns, the sequences $\left\{\underset{\sim}{f}^{(p)}\right\},\left\{\underset{\sim}{\theta}^{(p)}\right\}$ and $\left\{\underset{\sim}{\phi}^{(p)}\right\}$ are constructed which convergent to the solutions of Equations (17) – (19);

e) The processes is halted once the criteria $\max\left[\left\|\underset{\sim}{f}^{(p+1)}-\underset{\sim}{f}^{(p)}\right\|_{L_\infty},\left\|\underset{\sim}{\theta}^{(p+1)}-\underset{\sim}{\theta}^{(p)}\right\|_{L_\infty},\left\|\underset{\sim}{\phi}^{(p+1)}-\underset{\sim}{\phi}^{(p)}\right\|_{L_\infty}\right]<10^{-6}$ is met.

Finally, it is worth mentioning that the pentadiagonal matrix $G_{n\times n}$ is not diagonally dominant, in general, and therefore a direct method is more suitable. We have chosen the Guassian elimination technique with full pivoting, for this purpose in the present study.

4. Results and discussion

Current part is fermented for demonstrating the solution of the problem in the form of graphs and tables. Quantities of curiosity are the rate of shear stress, rate of heat, and mass transfer at the disks. We are confident to analyze the effect of various physical dimensionless constraints in the present work such as Magnetic field parameter M, Wall expansion ratio α, Reynolds number Re, Radiation parameter Nr, Prandtl number Pr, Casson parameter β, Eckert number Ec, Slip parameter λ, Schmidt number Sc, and the Chemical reaction parameter γ on temperature, velocity, and concentration distributions. It is essential to mention here that when the moving disks are approaching each other we take $\alpha < 0$ (contracting) and when the disks are moving away from each other we take $\alpha > 0$ (expanding). Here we shall also gain the knowledge for the numerical values of the rate of skin friction $f''(\pm 1)$, rate of heat transfer $\theta'(\pm 1)$, and rate of mass transfer $\phi'(\pm 1)$ at the upper and lower disk. Table 1 illustrates the validity of our numerical technique as the step size decelerate, which gives us self-assurance on our computational procedure. Table 2 demonstrates the effect of governing parameters on the coefficient of skin friction. It is found that the external magnetic field, Reynolds number, and Prandtl number augmented the shear stress whereas an opposite trend is seen for wall expansion ratio. Influence of rate of heat transfer on various parameters is depicted in Table 3. The rate of heat transfer amplifies with Reynolds number and Eckert number while a reverse trend is seen for radiation parameter, Casson parameter, and wall expansion ratio. Table 4 demonstrates the impact of Schmidt number and chemical reaction on rate of mass transfer. The rate of mass transfer shows a declining behavior with Schmidt number and chemical reaction for both the cases.

To authenticate the precision of our numerical method, an assessment for the calculated values of skin friction $f''(-1)$ at the lower disk with $\alpha = 1$ is made to that of Ghaffar et al. [25], and Jawad et al. [30] (for M = 0 and $\beta \to \infty$), in Figure 2 and close conformity is found. Therefore, we are sure that the current results are very precise. Figure 3 shows the streamlines of our governing flow problem.

Figures 4(a)-(d) depict the magnetic effect on the velocity and temperature distributions. In the middle part of the two moving disks, the velocity distribution reduces with M, and a contradictory behavior is obtained for temperature in both cases of wall expansion ratio $0 < \alpha$ and $\alpha > 0$. Physically, when a magnetic field is imposed on non-Newtonian fluid, viscosity of such fluids escalated due to the particle chain formation. Due to an augmentation in viscosity, the velocity of the fluid particle decelerates that can be perceived in the region $0 < \xi > 0.2$. Furthermore, induce external magnetic field gives kinetic energy (K.E) to the particles, and consequently velocity enhances near the disks. These results in Casson fluid flow between moving disks can be restricted by incorporating the external magnetic field that can be used in many control-based applications such as MHD power generation, and ion propulsion. Effect of Lorentz force is the creation of heat energy, enhancing the temperature of the fluid remarkably.

Impact of Reynolds number Re on the velocity, temperature, and concentration is illustrated in Figures 5(a)-(f). It should be observed that for velocity and concentration distribution, the Reynolds number has a contradictory effect of M, whereas a similar impact on temperature is observed, whether the disks are expanding ($\alpha > 0$) or contracting ($\alpha < 0$). Impact of α on distribution of velocity and temperature is shown in Figures 6(a)-(b). At the center of the disks, the velocity increases, and a maximum peak is attained at $(\xi = -0.4)$ after that the fashion of the velocity profile shows a declining behavior near the disk. Moreover, the temperature profiles are lowered near the disks and moves up for a smaller portion. Figures 7(a)-(d) represent the impact of the Prandtl number on velocity and temperature distribution. The velocity profile shows an increasing fashion with the growing values of Prandtl number in both cases. Physically, Prandtl number in dimensionless form is distinct as the ratio of the viscosity and fluid thermal diffusivity. And so, temperature profiles rise, when the Prandtl number increases. The dominant feature of viscosity with a rapid augmentation in Prandtl number is the main cause for temperature rises.

Figures 8(a)-(b) demonstrate the influence of the viscous dissipation on temperature for both cases $\alpha < 0$ and $\alpha > 0$. It is observed that the viscous dissipation astonishingly shows an increasing trend across the disks for the temperature distribution. Physically, Eckert's number is the relationship of K.E and change in enthalpy. Due to the drag forces, the heat energy is deposited in the fluid and K.E is augmented with the *Ec*. As a result, the fluid temperature grows. The impact of thermal radiation Nr on temperature is presented in Figures 8(c)-(d). It is noticeable that the initial values of Nr, the temperature rise but the large values of Nr, profiles start decreasing. The reason behind this fact is that when the values of thermal radiation increase, the absorption coefficient of the Casson fluid shows a declining trend. In these circumstances, the fluid between the surfaces of the disk absorbs a small amount of radiation, and hence the fluid temperature between the disks is bounded and vanishes remarkably.

In the governing equations, the presence of the parameter β shows a non-Newtonian rheological nature of Casson fluid. Figures 9(a)-(d) depict the effect of β on velocity and temperature distribution for $\alpha < 0$ and $\alpha > 0$. Velocity profiles increase with the enhancement in numerical values of the Casson parameter but a reverse trend is seen for temperature profiles. This interesting phenomenon explains that the Casson parameter is distinct to demonstrate the strength of yield stress and viscous forces. Strength of yield stress decreases with β. Therefore, under a particular pressure gradient, the non-Newtonian Casson fluid flows more freely. That is why the fluid velocity is augmented, the convection of heat transfer is strengthened because of better mixing of the fluid, and the outcome is the lessening of fluid temperature. Figures 10(a) and 10(b) demonstrate the influence of Schmidt number and chemical reaction on the concentration distribution. Schmidt number has a converse relationship with mass diffusion and augmenting values lead to a decline in concentration. The rate of mass transfer shows a declining behavior with the increase in chemical reaction parameters at both disks. Velocity distribution for numerous values of slip parameter is seen in Figures 11(a) and 11(b). The velocity distribution reduces with the enhancement in slip factor.

5. Conclusions

In the current work, a mathematical model has been developed to study the convective driven unsteady non-Newtonian Casson fluid flow between two orthogonally moving disks. The Quasilinearization technique was used to obtain the numerical solution of the flow and heat transfer phenomenon. Influence of the encountered parameters has been discussed in detail through graphs and tables. During the thorough analysis of the problem, following points have been revealed:

1. For the case of purely Newtonian flow and in the absece of magnetic force (that is, M = 0 and $\beta \to \infty$), our current numerical results are found in excellent conformity with the existing scientific literature (Ghaffar et al. [25] and Jawad et al. [30]).
2. The absence of no slip boundary condition may be regarded as an extra ordinary situation for controlling the flow and shear stress in moving disks. Therefore, the slip effects cannot be simply ignored.
3. Velocity profile enhances in the middle of the domain and reduces near the disks, for the case when the disk expansion ratio is positive (which corresponds to the situation when the two disks are moving away). However, an opposite trend is encountered when the two disks are approaching each other.
4. All the governing parameters remarkably enhance the fluid temperature at a central region between the disks.
5. Shear stress at the two disks is raised with the parameters $M, \mathrm{Re}, \text{and}\, \mathrm{Pr}$ whereas an opposite trend is noted for α whether the disks are receding or approaching.

6. Heat transfer rate at either of the disks is found to be an increasing function of the Prandtl number and the Eckert number. A reverse trend is however encountered for the thermal radiation and the casson nature of the fluid.
7. Finally, a significant decrease in the concentration profile and the mass transfer rate (at the disks) has been noticed for both the Scmidth number and the chemical reaction paarameter.

6. Nomenclature

Dimensional Parameter	**Non-Dimensional Parameter**
B_0 Applied magnetic field	α Wall expansion ratio
c_p Specific heat at constant pressure	ξ Similarity variable
$L(t)$ Distance between disk	F Dimensionless stream function
σ_e Electrical conductivity	f' Dimensionless velocity
h_1, h_2 Coefficient of convective heat transfer	θ Dimensionless temperature
$\tilde{e}_{ij}$ the $(i,j)^{th}$ component of deformation rate	ϕ Dimensionless concentration
$\tilde{\pi}$ product of the component of deformation rate	υ Kinematic viscosity
P_y Fluid yield stress	σ^* Stefan-Boltzmann constant
H Wall permeability	k^* Mean absorption coefficient
T Fluid temperature	C_f Local Skin friction coefficient
C Fluid concentration	Nu_x Local Nusselt number
T_1, T_2 Fixed temperatures	Sh_x Local Sherwood number
C_1, C_2 Fixed concentrations	M Magnetic field parameter
u_1, u_2, u_3 Velocity components of fluid	Ec Eckert number
r, θ, z Cylindrical polar coordinates	β Casson parameter
$\tilde{\alpha}$ thermal conductivity	$\Pr$ Prandtl number
ρ Density of the fluid	λ Slip parameter
$\tilde{\mu}_B$ Dynamic viscosity of a non-Newtonian fluid	Sc Schmidt number
	γ Chemical reaction parameter
	Re Reynolds number
	Nr Radiation parameter

7. REFERENCES

[1] Joseph, M., Chong, Z., & Christopher, A.D. "Two Dimensional Viscous Flows between Slowly Expanding or Contracting Walls with Weak Permeability", J. Biomech., **35**, pp. 1399-1403 (2002).

[2] Von Karman, T., "Uber laminare and turbulente Reibung", Zeit. Angew. Math. Mech., (1921).

[3] Abbas, Z., Rauf, A., & Shehzad, S.A., et al., "Cattaneo-Christov heat and mass flux models on time-dependent swirling flow through oscillatory rotating disk", Scientia Iranica., **28**, pp. 1329-1341 (2021).

[4] Abbasi, A., Mabood, F., & Farooq, W., et al., "Bio convective flow of viscoelastic Nanofluid over a convective rotating stretching disk", Int. J. of Heat and Mass Tranf., **119**, 104921 (2020).

[5] Mair, K., Salahuddin, T., & Stephen, S.O. "Thermo-physical characteristics of liquids and gases near a rotating disk", Chaos Sol. and Fract., **141**, 110304 (2020).

[6] Muhammad, S., Nazir, U., & Chu, Y.M., et al., "Bioconvection phenomenon for the boundary layer flow of magnetohydrodynamic Carreau liquid over a heated disk", Scientia Iranica., **28**, pp. 1896-1907 (2021).

[7] Adil, S., Farwa, H., & Tasawar, H., "Partial slip in Darcy-Forchheimer carbon nanotubes flow by rotating disk", Int. J. of Heat and Mass Tranfer., **116**, 104641 (2020).

[8] Mamatha, U., Devi, R.L., & Raju, C.S., et al., "Magnetohydrodynamic nonlinear thermal convection nanofluid flow over a radiated porous rotating disk with internal heating", J. of Ther. Ana. and Calo., **143**, pp. 1973-1984 (2021).

[9] Jawad, A., Masood, K., & Latif, A., "Stagnation point flow of Maxwell nanofluid over a permeable rotating disk with heat source/sink", J. of Mol. Liq., **287**, 110853 (2019).

[10] Babu, B.H., Rao, P.S., & Reddy, M.G., et al., "Numerical modelling of activation energy and hydromagnetic non-Newtonian fluid particle deposition flow in a rotating disc" J. of Pro. mech. Engg., **237,** 10.1177, (2021).

[11] Ali, K., Ahmad, A., & Ahmad, S., et al., "A Numerical approach for analyzing the Electromagnetohydrodynamic flow through a rotating microchannel" Arab. J. of Sci. & Engg., **48**, pp. 3765-3781, (2023).

[12] Syed, M.R., Hyun, M.K., & Taseer, M., et al., "Numerical study for slip flow of Reiner-Rivlin nanofluid due to a rotating disk", Int. J. of Heat and Mass Tranfer, **116**, 104643 (2020).

[13] Iqbal, M.F., Ali, K., & Ashraf, M., "Heat and mass transfer analysis in unsteady titanium dioxide nanofluid between two orthogonally moving porous coaxial disks: a numerical study", Cand. J. Phy., **93**, (2014).

[14] Iqbal, M.F., Ahmad, S., & Ali, K., et al., "Analysis of heat and mass transfer in unsteady nanofluid flow between moving disk with chemical reaction- A numerical study", Heat Transfer Research, pp. 1403-1417 (2018).

[15] Masood, K., Jawad, A., & Wajid, A., "Thermal analysis for the radiative flow of magnetized Maxwell fluid over a vertically moving rotating disk", J. of Ther. Anal. And Calo., **143**, pp. 4081-4094, (2021).

[16] Muhammad, S., Muhammad, B., Muhammad, A.K., et al., "Fractional analysis of viscous fluid flow with heat and mass transfer over a flexible rotating disk", CMES, **123**, pp. 377-400 (2020).

[17] Taza, G., Kashif, U., & Muhammad, I.A., et al., "Hybrid nanofluid flow within the conical gap between the cone and the surface of a rotating disk", Scientfic Report, **11**, 1180 (2021).

[18] Talat, R., Mustafa. M., & Asif, F., "Modeling heat transfer in fluid flow near a decelerating rotating disk with variable fluid properties", Int. J. of Heat and Mass Tranf., **116**, 104673 (2020).

[19] Khan, M.R., Pan, K., & Khan, A., et al., "Dual solutions for mixed convection flow of $SiO_2-Al_2O_3$/water hybrid nanofluid near the stagnation point over a curved surface", Physica A: Stat. Mech. App., **547**, 123959 (2020)..

[20] Hussain, A., Alshbool, M.H., & Abdussattar, A., et al., “A computational model for hybrid nanofluid flow on a rotating surface in the existence of convective condition”, Case Studies in Thermal Engg., **26**, 101089 (2021).
[21] Li, Y., Alshbool, M.H., & Yu-Pei, K., et al., “Heat and mass transfer in MHD Williamson nanofluid flow over an exponentially porous stretching surface”, Case Studies in Thermal Engg., **26**, 100975 (2021)..
[22] Khan, M.R., Pan, K., & Khan, A., et al., “Comparative study on heat transfer in CNTs-water nanofluid over a curved surface”, Int. Comm. Heat and Mass Transfer, **116**, 104707 (2020).
[23] Naveen, K., Punith, G., & Gireesha, B.J., et al., “Non-Newtonian hybrid nanofluid flow over vertically upward/downward-moving rotating disk in a Darcy–Forchheimer porous medium”, The Eur. Phy. J. Sp. Top., **230,** pp. 1227-1237 (2021).
[24] Zhao, T.H., Khan, M.I., & Chu, Y.M., “Artificial neural networking (ANN) analysis for heat and entropy generation in flow of non-Newtonian fluid between two rotating disks”, Mathematical Methods in the applied science, pp. 3012-3030 (2023).
[25] Ghaffar, M., Ali, K., & Yasmin, A., et al., “Unsteady flow between two orthogonally moving porous disks”, J. of Mechanics, **31**, pp. 147-151 (2015).
[26] Shehzad, S.A., Mabood, F., & Rauf, A., et al., “Rheological features of non-Newtonian nanofluids flow induced by stretchable rotating disk”, Phys. Scr., **96,** 035210, (2021).
[27]Ali, K., Ahmad, A., & Ahmad, S., et al., “Peristaltic pumping of MHD flow through a porous channel: biomedical engineering application”, Waves in Rand. And Complex Media, 17455030, (2023).
[28] Shamshuddin, M.D., Akkurt, & N., Saeed, A., et al., “Radiation mechanism on dissipative ternary hybrid nanoliquid flow through rotating disk encountered by Hall currents: HAM solution”, Alexandria Engg. J., **65**, pp. 543-559, (2023).
[29] Ahmad, S., Ahmad, A., & Ali, K., et al., “ Effect of non-Newtonian flow due to thermally-dependent properties over an inclined surface in the presence of chemical reaction, Brownian motion and thermophoresis”, Alexandria Engg. J. **60**, pp. 4931-4945, (2021).
[30] Jawad, R., Rohni, A.M., & Omer, Z., “Unsteady flow of Casson fluid between two orthogonally moving porous disks: A numerical investigation”, Communication in Numerical Analysis, 55996581 (2017).

8. List of Figures and Tables Captions

Figure 9. Variation of $f'(\zeta)$ and $\theta(\zeta)$ with different values of β for $\alpha < 0$ and $\alpha > 0$.

Figure 10. Variation of $\phi(\zeta)$ with different values Sc and γ of for $\alpha < 0$.

Figure 11. Variation of $f'(\zeta)$ with different values λ for $\alpha < 0$ and $\alpha > 0$

Table 1. Dimensionless velocity $f(\xi)$ on three different grid sizes and extrapolated values for $\mathrm{Re} = -2, M = 2, \beta = 10, \mathrm{Pr} = \alpha = Sc = Nr = \lambda = 1,\ Ec = 0.1, \delta = 2,\ \varepsilon = 0.5, \text{and}\ \gamma = 1.5.$

Table 2. Numerical values of Skin friction coefficient for $\mathrm{Re} = -2, M = 2, \beta = 10,\ Ec = 0.1, \delta = 2,$ $\mathrm{Pr} = \alpha = Sc = Nr = \lambda = 1,\ \varepsilon = 0.5, \text{and}\ \gamma = 1.5.$

Table 3. Numerical values of Nusselt number for $\mathrm{Re} = -2, M = 2, \beta = 10, \mathrm{Pr} = \alpha = Sc = Nr = \lambda = 1,$ $\mathrm{Re} = -2, M = 2, \beta = 10,\ Ec = 0.1, \delta = 2,\ \mathrm{Pr} = \alpha = Sc = Nr = \lambda = 1,\ \varepsilon = 0.5, \text{and}\ \gamma = 1.5.$

Table 4. Numerical values of Sherwood number for $\mathrm{Re} = -2, M = 2, \beta = 10,\ Ec = 0.1, \delta = 2,$ $\mathrm{Pr} = \alpha = Sc = Nr = \lambda = 1,\ \varepsilon = 0.5, \text{and}\ \gamma = 1.5.$

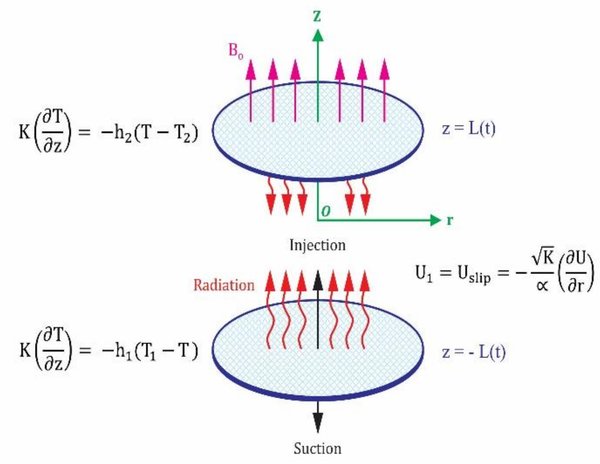

Figure 1. Geometry of Model Problem

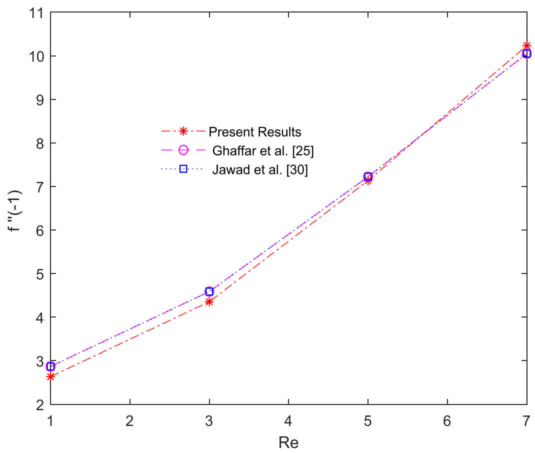

Figure 2. Comparison of skin friction $f''(-1)$ with different Re for $M = 0$ and $\beta \to \infty$.

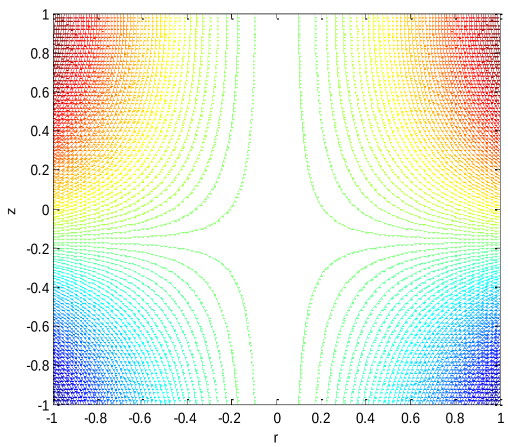

Figure 3. Streamlines for the problem at $\mathrm{Re} = -2, M = 2, \beta = 10, \alpha = 1, \delta = 2, \varepsilon = 0.5.$

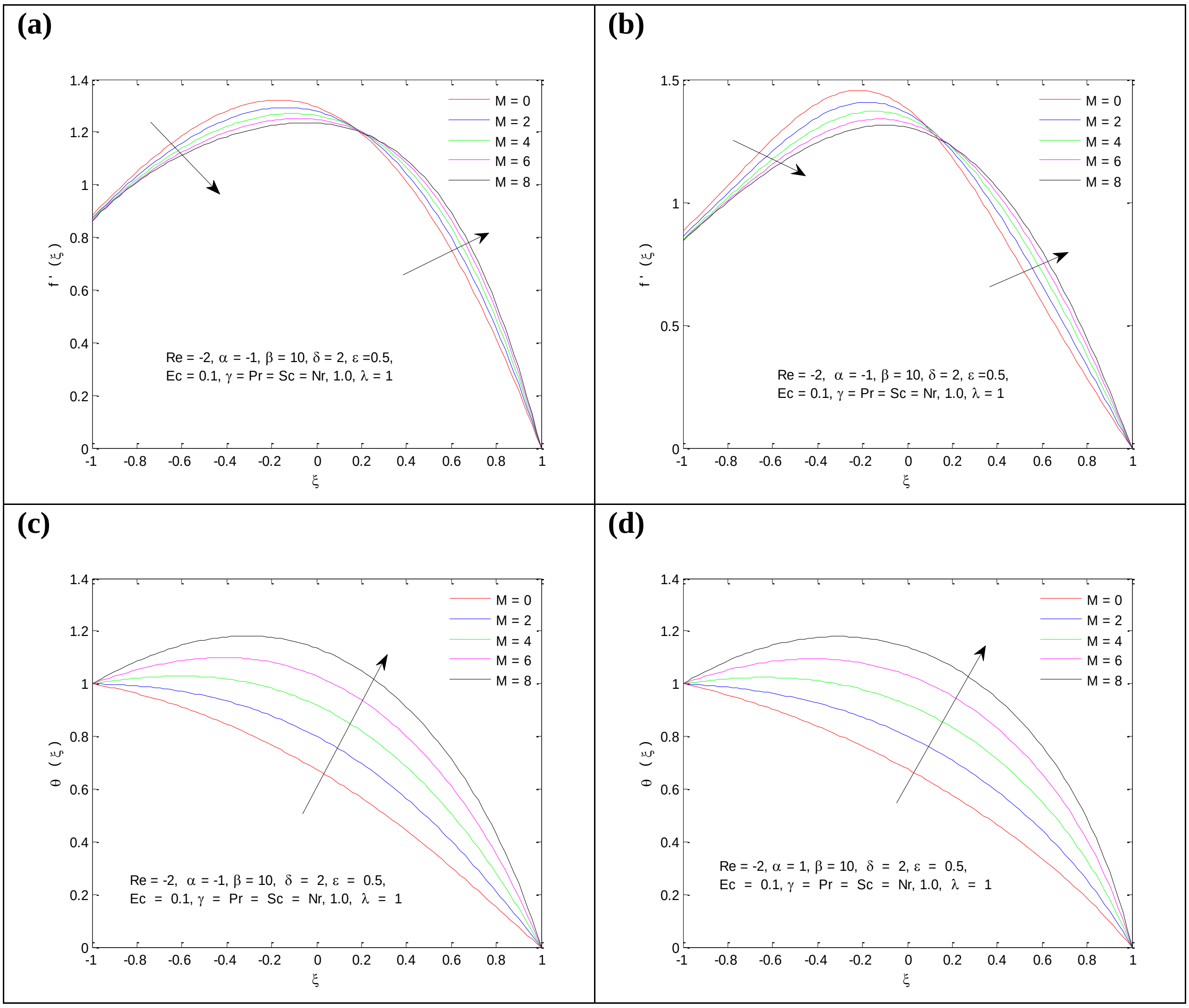

Figure 4. Variation of $f'(\zeta)$ and $\theta(\zeta)$ with different values of M for $\alpha < 0$ and $\alpha > 0$

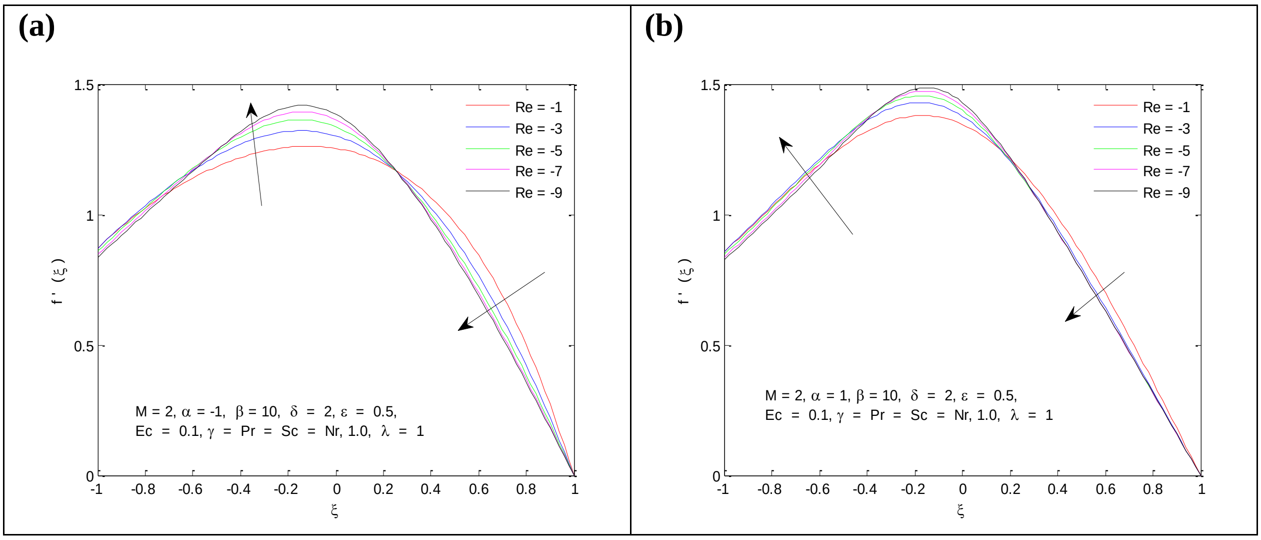

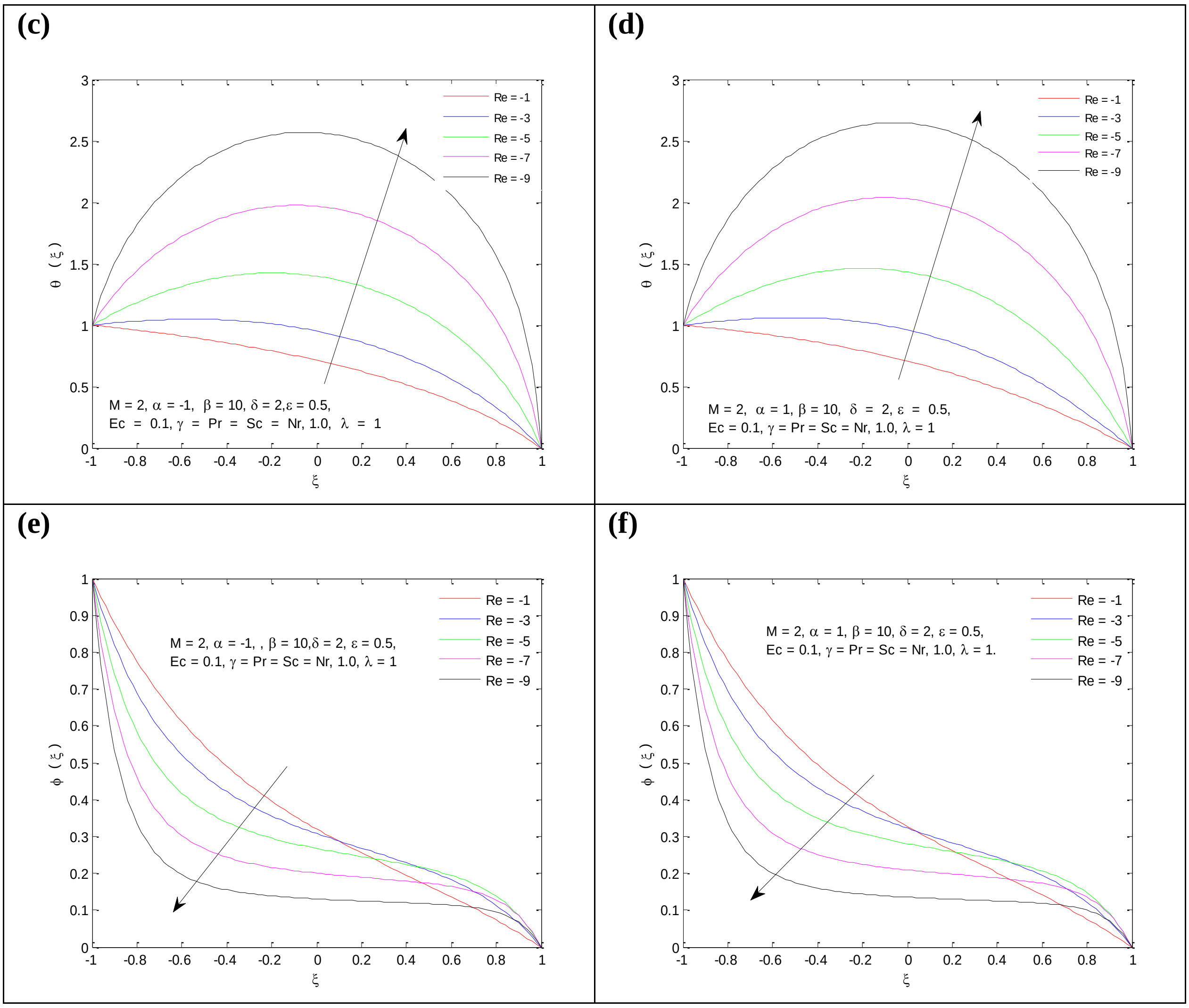

Figure 5. Variation of $f'(\zeta), \theta(\zeta)$ and $\phi(\zeta)$ with Re for $\alpha < 0$ and $\alpha > 0$

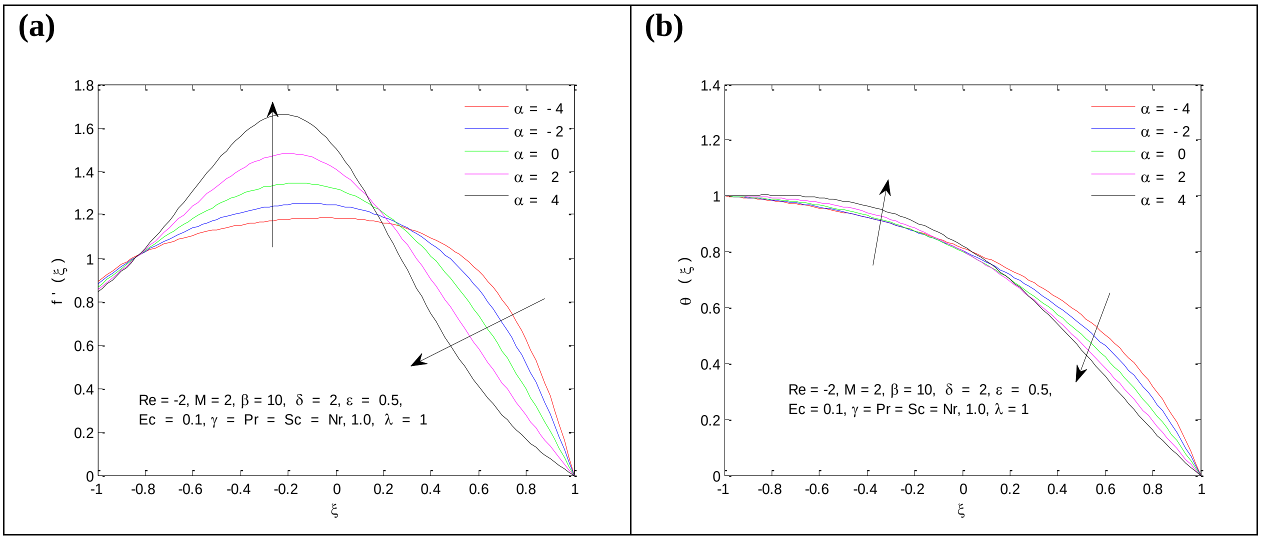

Figure 6. Variation of $f'(\zeta)$ and $\theta(\zeta)$ with $\alpha < 0$ and $\alpha > 0$

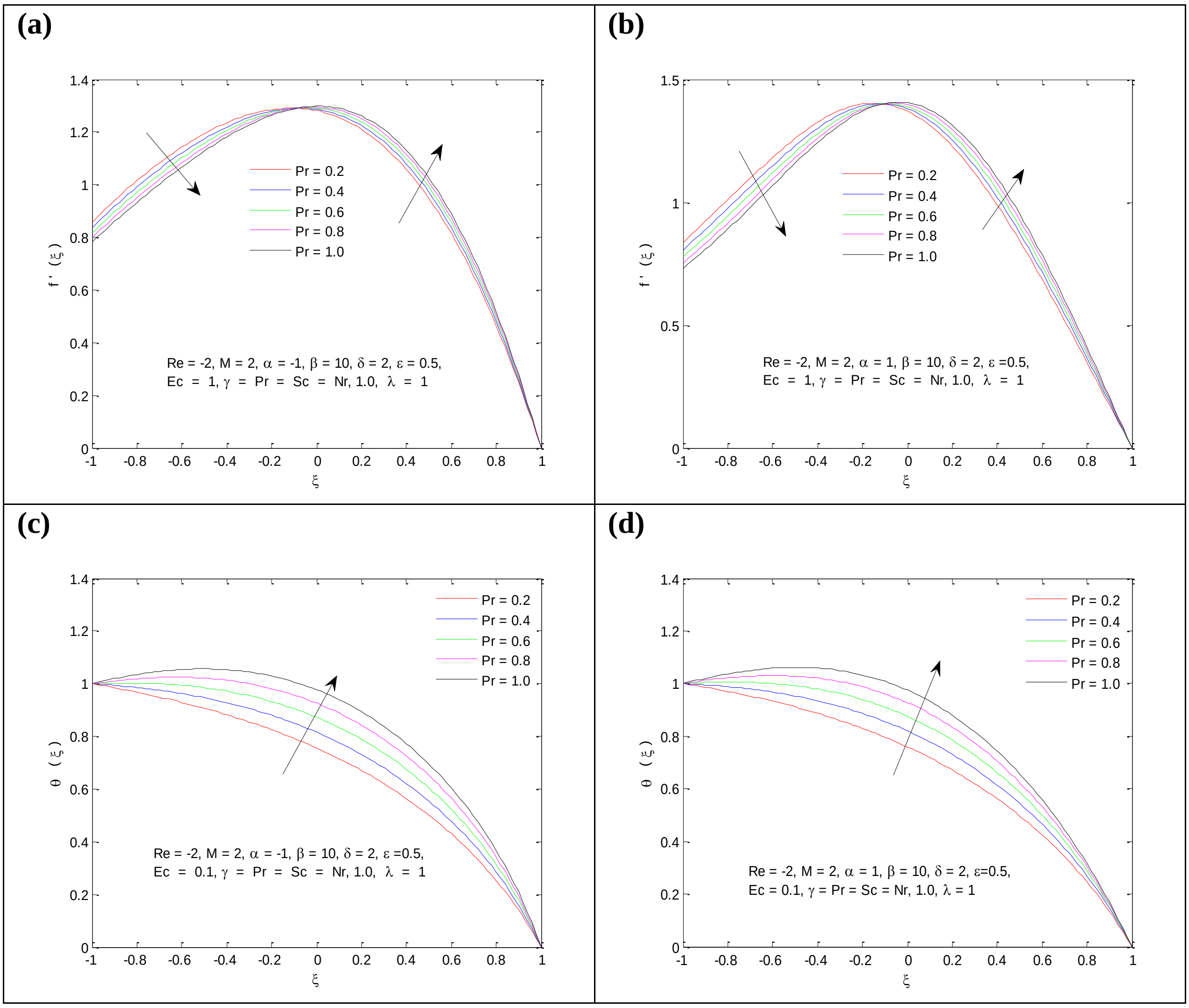

Figure 7. Variation of $f'(\zeta)$ and $\theta(\zeta)$ with different values of Pr for $\alpha < 0$ and $\alpha > 0$

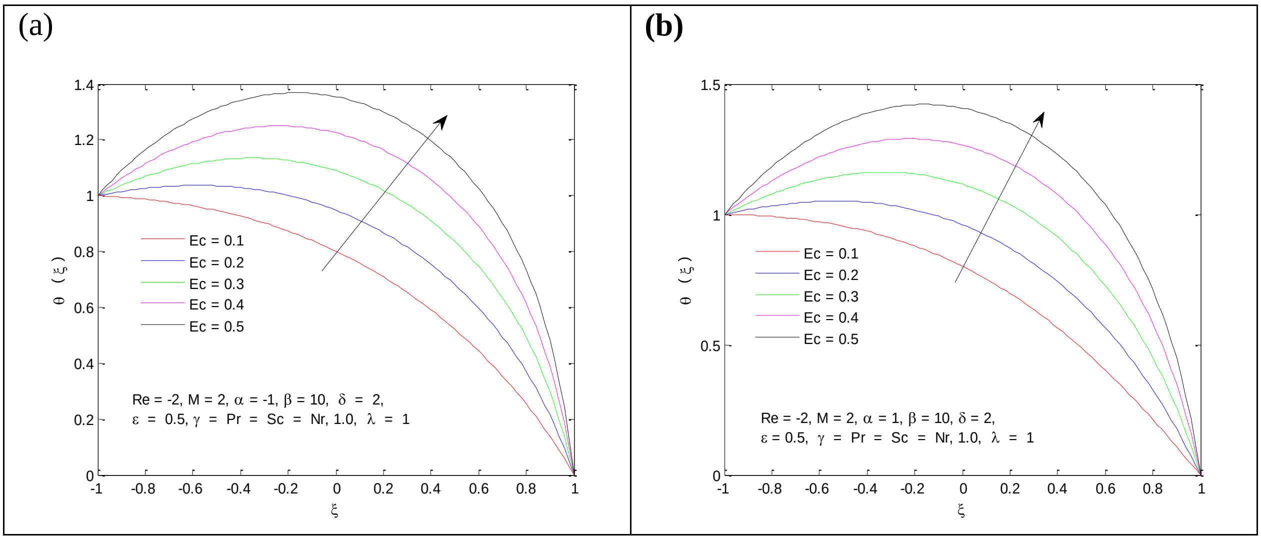

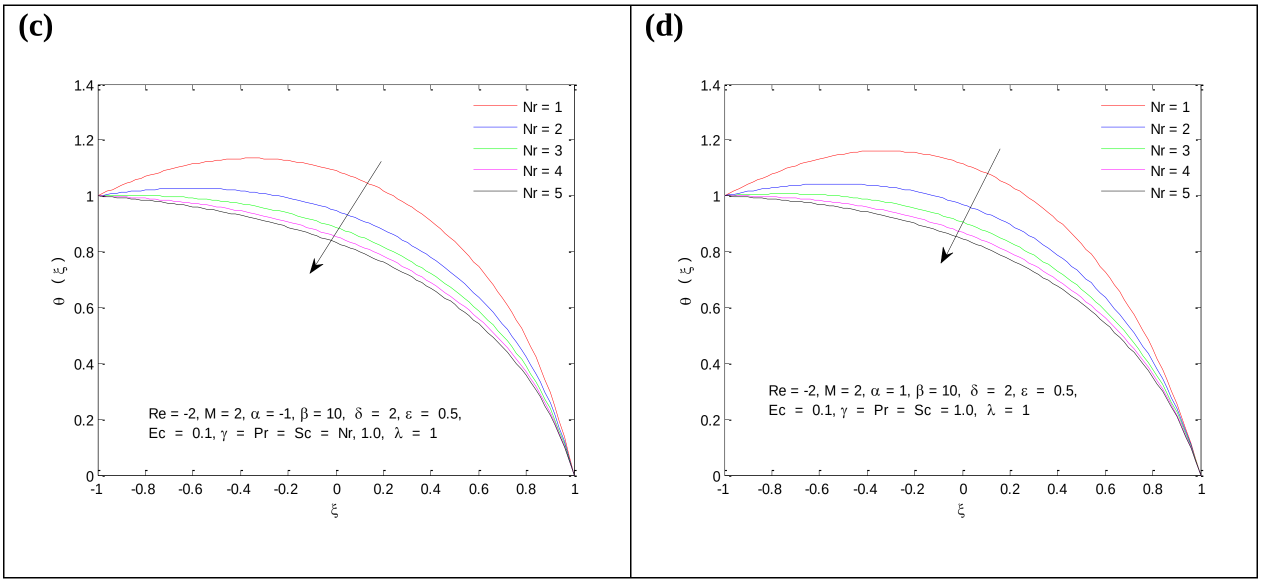

Figure 8. Variation of $\theta(\zeta)$ with Ec and Nr for $\alpha < 0$ and $\alpha > 0$

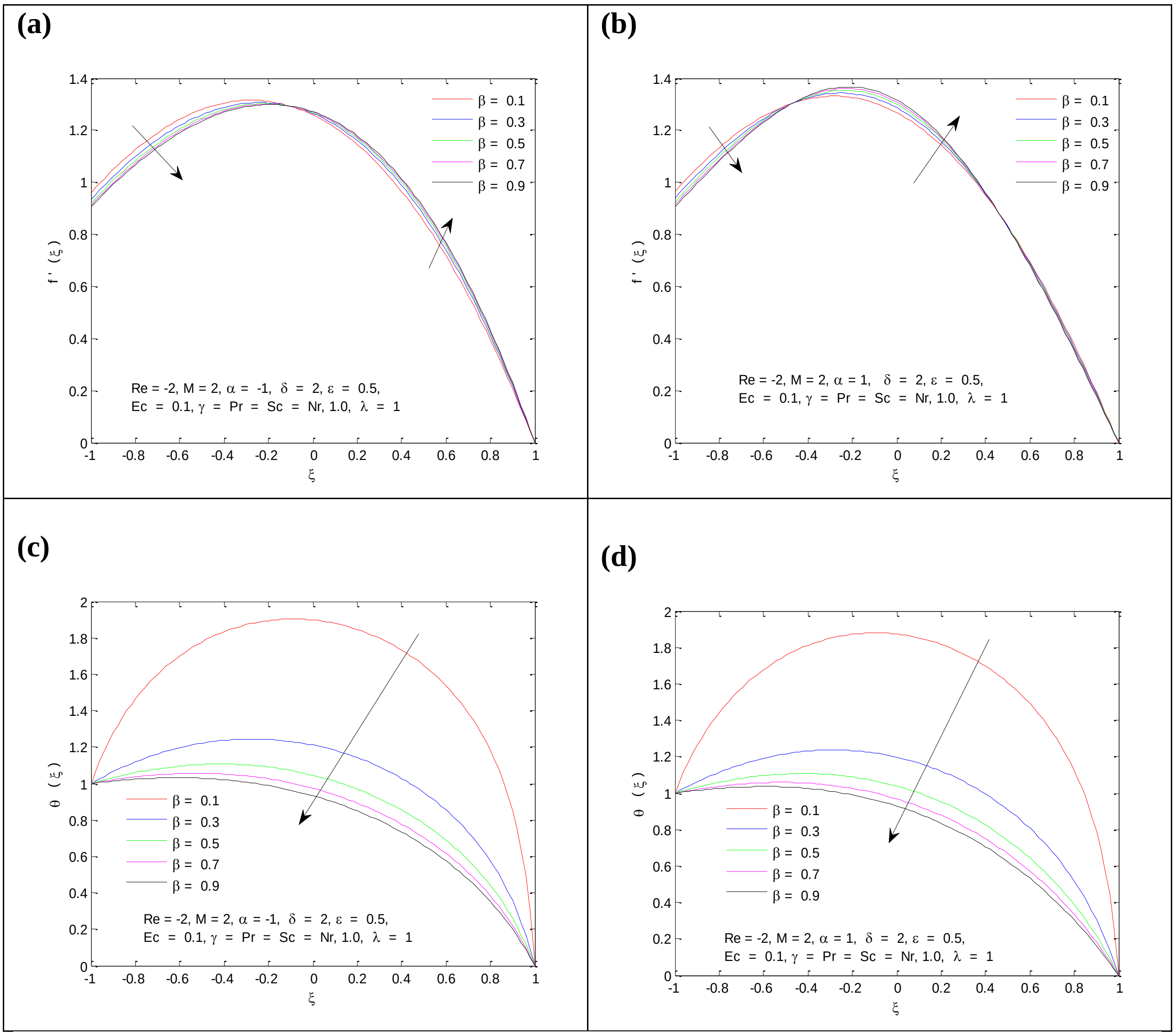

Figure 9. Variation of $f'(\zeta)$ and $\theta(\zeta)$ with different values of β for $\alpha < 0$ and $\alpha > 0$

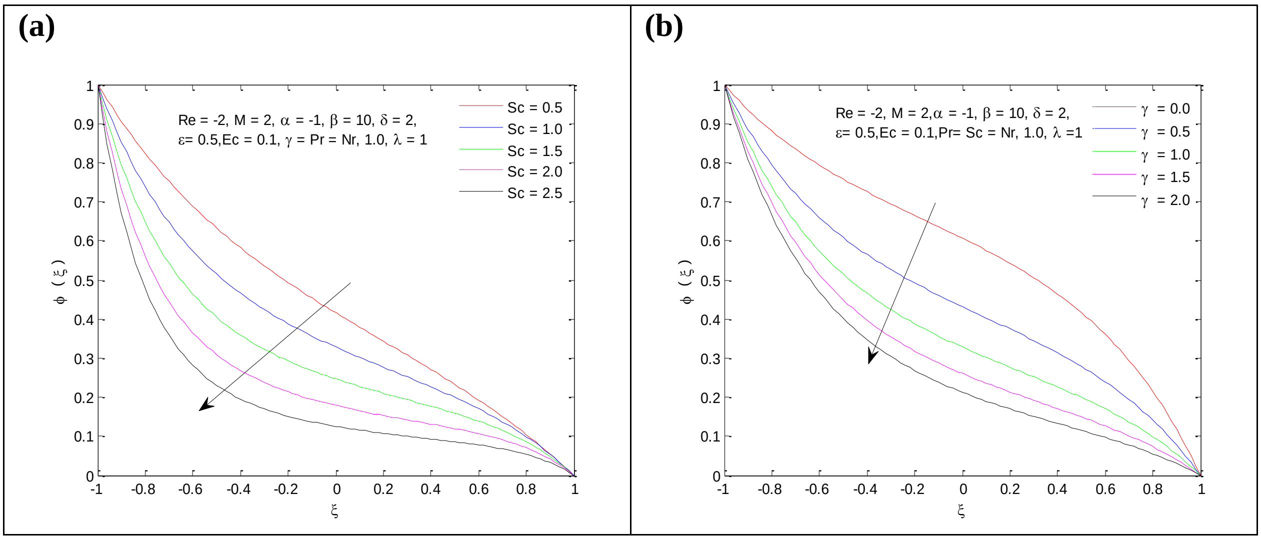

Figure 10. Variation of $\phi(\zeta)$ with different values Sc and γ of for $\alpha < 0$

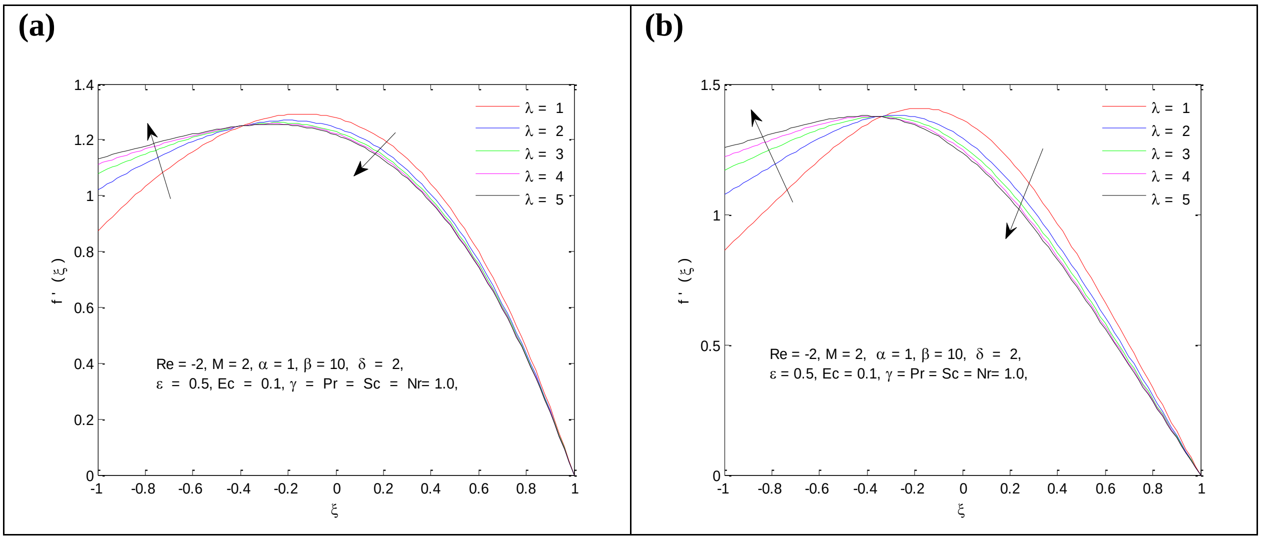

Figure 11. Variation of $f'(\zeta)$ with different values λ for $\alpha < 0$ and $\alpha > 0$

	$f(\xi)$			
ξ	H	h/2	h/4	Extrapolated values
-1	-1	-1	-1	-1
-0.8	-0.959547	-0.959556	-0.959966	-0.960103
-0.6	-0.833905	-0.833907	-0.835590	-0.836152
-0.4	-0.621507	-0.833907	-0.625271	-0.626529
-0.2	-0.333514	-0.333504	-0.339808	-0.341910
0	-4.798745e-12	-1.363486e-11	-0.008500	-0.011333
0.2	0.333514	0.333504	0.324006	0.320840
0.4	0.621507	0.621498	0.612620	0.609660
0.6	0.833905	0.833907	0.827090	0.824817
0.8	0.959547	0.959556	0.955795	0.954541
1	1	1	0.999902	0.999870

Table 1. Dimensionless velocity $f''(\xi)$ on three different grid sizes and extrapolated values for $\mathrm{Re}=-2, M=2, \beta=10, \mathrm{Pr}=\alpha=Sc=Nr=\lambda=1,\ Ec=0.1, \delta=2,\ \varepsilon=0.5, \text{and}\ \gamma=1.5.$

							$\alpha=1$		$\alpha=-1$	
M	Re	α	Pr	β	λ	δ	$f''(1)$	$f''(-1)$	$f''(1)$	$f''(-1)$
0							-1.36578	0.89062	-2.24390	0.87604
2							-1.67028	0.86443	-2.53757	0.86183
4							-1.94601	0.84979	-2.80568	0.85260
6							-2.19960	0.84114	-3.05321	0.84635
8							-2.43532	0.83585	-3.28363	0.84197
	-1						-1.81962	0.85901	-2.92340	0.85595
	-3						-1.60438	0.86275	-2.29047	0.86259
	-5						-1.57048	0.85142	-2.03006	0.85553
	-7						-1.57799	0.83865	-1.91471	0.84470
	-9						-1.58973	0.82898	-1.85329	0.83536
		-4					-4.10643	0.85580	-4.10643	0.85580
		-2					-3.02968	0.86014	-3.02968	0.86014
		0					-2.08301	0.86324	-2.08301	0.86324
		2					-1.30256	0.86556	-1.30256	0.86556
		4					-0.70713	0.86869	-0.70713	0.86869
			0.2				-1.65266	0.87191	-2.51411	0.86779
			0.4				-1.65814	0.86972	-2.52060	0.86617
			0.6				-1.66286	0.86776	-2.52666	0.86464
			0.8				-1.66688	0.86601	-2.53230	0.86320
			1.0				-1.67028	0.86443	-2.53757	0.86183
				0.1			-2.00292	0.94731	-2.15158	0.94105
				0.3			-1.92493	0.92915	-2.26321	0.91826
				0.5			-1.87091	0.91749	-2.32457	0.90559
				0.7			-1.83367	0.90907	-2.36468	0.89730
				0.9			-1.80678	0.90270	-2.39304	0.89143
					1		-1.67028	0.86443	-2.53757	0.86183
					2		-1.51742	0.54107	-2.43131	0.50552
					3		-1.45507	0.39300	-2.38972	0.35820
					4		-1.42141	0.30858	-2.36758	0.27783
					5		-1.40037	0.25412	-2.35383	0.22726
						1	-1.55095	0.91471	-2.41272	0.89931
						2	-1.67028	0.86443	-2.53757	0.86183
						3	-1.79523	0.81367	-2.66627	0.82404
						4	-1.92644	0.76235	-2.79915	0.78591
						5	-2.06460	0.71041	-2.93659	0.74739

Table 2. Numerical values of Skin friction coefficient for $\mathrm{Re}=-2, M=2, \beta=10,\ Ec=0.1, \delta=2,$ $\mathrm{Pr}=\alpha=Sc=Nr=\lambda=1,\ \varepsilon=0.5, \text{and}\ \gamma=1.5.$

							$\alpha=1$		$\alpha=-1$	
M	Re	α	Pr	β	Nr	Ec	$\theta'(1)$	$\theta'(-1)$	$\theta'(1)$	$\theta'(-1)$
0							-0.74209	-0.16129	-1.04910	-0.19291
2							-1.10104	-0.02010	-1.52327	-0.04223
4							-1.55181	0.13100	-2.10464	0.12250
6							-2.10377	0.29620	-2.80110	0.30408
8							-2.76461	0.47794	-3.61795	0.50437
	-1						-0.98274	-0.16610	-1.32079	-0.18986
	-3						-1.46206	0.21372	-2.02551	0.19181
	-5						-3.30923	1.07308	-4.31252	1.03761
	-7						-9.12029	3.02801	-10.62976	2.89487
	-9						-23.74409	7.32225	-25.20129	6.87779
		-4					-2.35951	-0.06456	-2.35951	-0.06456
		-2					-1.77586	-0.05085	-1.77586	-0.05085
		0					-1.29813	-0.03210	-1.29813	-0.03210
		2					-0.93208	-0.00578	-0.93208	-0.00578
		4					-0.67564	0.03214	-0.67564	0.03214
			0.2				-1.31351	-0.18824	-1.39318	-0.19722
			0.4				-1.27435	-0.14008	-1.43842	-0.15547
			0.6				-1.22399	-0.09624	-1.47468	-0.11577
			0.8				-1.16535	-0.05636	-1.50273	-0.07805
			1.0				-1.10104	-0.02010	-1.52327	-0.04223
				0.1			-15.16779	3.22801	-17.60692	3.53405
				0.3			-3.79045	0.66507	-4.81522	0.71112
				0.5			-2.47426	0.34499	-3.22708	0.35601
				0.7			-2.00340	0.22459	-2.64944	0.22324
				0.9			-1.76429	0.16178	-2.35384	0.15434
					1		-1.10104	-0.02010	-1.52327	-0.04223
					2		-1.51060	-0.09108	-1.80767	-0.10869
					3		-1.71418	-0.12237	-1.93800	-0.13617
					4		-1.83339	-0.13991	-2.01200	-0.15114
					5		-1.91124	-0.15111	-2.05957	-0.16055
						0.1	-1.10104	-0.02010	-1.52327	-0.04223
						0.2	-1.92089	0.18974	-2.55085	0.16297
						0.3	-3.02411	0.43666	-3.84794	0.40024
						0.4	-4.45969	0.72673	-5.44258	0.67352
						0.5	-6.26305	1.06534	-7.35016	0.98615

Table 3. Numerical values of Nusselt number for $\mathrm{Re}=-2, M=2, \beta=10, \mathrm{Pr}=\alpha=Sc=Nr=\lambda=1,$ $\mathrm{Re}=-2, M=2, \beta=10,$ $Ec=0.1, \delta=2,$ $\mathrm{Pr}=\alpha=Sc=Nr=\lambda=1,$ $\varepsilon=0.5,$ and $\gamma=1.5.$

			$\alpha=-1$		$\alpha=1$	
Re	Sc	γ	$\phi'(1)$	$\phi'(-1)$	$\phi'(1)$	$\phi'(-1)$
-1			-0.31298	-1.56620	-0.30226	-1.57332
-3			-0.57354	-2.43762	-0.53613	-2.46209
-5			-0.78168	-3.70103	-0.73268	-3.73126
-7			-0.80686	-5.38065	-0.76427	-5.40449
-9			-0.66960	-7.36157	-0.63976	-7.37498
	0.5		-0.48857	-1.17611	-0.47285	-1.18655
	1.0		-0.43852	-1.95907	-0.41391	-1.97557
	1.5		-0.36800	-2.82149	-0.34045	-2.84050
	2.0		-0.29338	-3.73898	-0.26680	-3.75797
	2.5		-0.22501	-4.69238	-0.20146	-4.70964
		0.0	-1.30136	-0.71834	-1.22475	-0.76648
		0.5	-0.85209	-1.28317	-0.80320	-1.31442
		1.0	-0.59782	-1.66735	-0.56399	-1.68946
		1.5	-0.43852	-1.95907	-0.41391	-1.97557
		2.0	-0.33193	-2.19624	-0.31339	-2.20900

Table 4. Numerical values of Sherwood number for $\mathrm{Re}=-2, M=2, \beta=10$, $Ec=0.1, \delta=2$, $\mathrm{Pr}=\alpha=Sc=Nr=\lambda=1$, $\varepsilon=0.5$, and $\gamma=1.5$.

Declaration

Authors Contribution

Conceptualization, Shahzad Ahmad and Anique Ahmad; Methodology, Shahzad Ahmad; Software, Kashif Ali; Data curation, Kashif Ali and Anique Ahmad.; Writing—original draft preparation, Anique Ahmad; Writing—review and editing, Anique Ahmad; Supervision, Shahzad Ahmad and Kashif Ali;

Funding

There is no financial support to carry out this research.

Data availability statement

All the relevant material is available upon request.

Declaration of competing interest

The authors declare that they have no known competing financial interests or personal relationships that could have appeared to influence the work reported in this paper.

Conflicts of interest

On behalf of all authors, the corresponding author states that there is no conflict of interest.

Authors technical bio

Dr. Kashif Ali is Assistant Professor (Applied Mathematics) in the Department of Basic Sciences and Humanities, Muhammad Nawaz Sharif University of Engineering and Technology, Multan, Pakistan. He has published over 40 papers in peer-reviewed journals. CFD and particularly the solution of nonlinear differential equations arising from the modeling of non-Newtonian flows in various configurations are his main areas of research interest.

Mr. Anique Ahmad is currently PhD candidate in the Centre for Advanced Studies in Pure and Applied Mathematics, Bahauddin Zakariya University, Multan, Pakistan. He obtained his M.Phil. and M.Sc. (Mathematics) degrees from the same university in the years 2017 and 2014, respectively. His research interests include the numerical solution of nonlinear problems, mathematical modeling and Computational Fluid Dynamics (CFD).

Dr. Shahzad Ahmad is the Assistant Professor in Centre for Advanced Studies in Pure and Applied Mathematics, Bahauddin Zakariya University, Multan, Pakistan. He has published more than 30 papers in international journals. He teaches undergraduate and graduate courses in the department. His areas of interest are the fluid structure interaction, internal combustion engines and internal fluid flows.